

Integrated Super-Resolution Sensing and Communication with 5G NR Waveform: Signal Processing with Uneven CPs and Experiments

(Invited Paper)

Chaoyue Zhang*, Zhiwen Zhou*, Huizhi Wang*, and Yong Zeng*[†]

*National Mobile Communications Research Laboratory, Southeast University, Nanjing 210096, China

[†]Purple Mountain Laboratories, Nanjing 211111, China

Email: 220211013@seu.edu.cn, 220220790@seu.edu.cn, wanghuizhi@seu.edu.cn, yong_zeng@seu.edu.cn.

Abstract—Integrated sensing and communication (ISAC) is a promising technology to simultaneously provide high-performance wireless communication and radar sensing services in future networks. In this paper, we propose the concept of *integrated super-resolution sensing and communication* (ISSAC), which uses super-resolution algorithms in ISAC systems to achieve extreme sensing performance for those critical parameters, such as delay, Doppler, and angle of the sensing targets. Based on practical fifth generation (5G) New Radio (NR) waveforms, the signal processing techniques of ISSAC are investigated and prototyping experiments are performed to verify the achievable performance. To this end, we first study the effect of uneven cyclic prefix (CP) lengths of 5G NR orthogonal frequency division multiplexing (OFDM) waveforms on various sensing algorithms. Specifically, the performance of the standard Periodogram based radar processing method, together with the two classical super-resolution algorithms, namely, Multiple Signal Classification (MUSIC) and Estimating Signal Parameter via Rotational Invariance Techniques (ESPRIT) are analyzed in terms of the delay and Doppler estimation. To resolve the uneven CP issue, a new structure of steering vector for MUSIC and a new selection of submatrices for ESPRIT are proposed. Furthermore, an ISSAC experiment platform is setup to validate the theoretical analysis, and the experimental results show that the performance degradation caused by unequal CP length is insignificant and high-resolution delay and Doppler estimation of the target can be achieved with 5G NR waveforms.

I. INTRODUCTION

Integrated sensing and communication (ISAC) is an emerging technology that received significant research interest recently [1], which aims to provide high-performance wireless communication and ubiquitous radar sensing service simultaneously. Extensive research efforts have been devoted to the theoretical analysis and optimization in terms of waveform design [2] [3], seamless sensing coverage [4], beamforming [5], beam alignment [6] [7] and information-theoretical limits analysis [8]–[10]. On the other hand, practical signal processing techniques for specific sensing tasks such as target detection or parameter estimation have received relatively less attention for ISAC.

In particular, one of the important tasks for ISAC is to estimate the critical parameters of the sensing targets, such as angle of arrival (AoA), propagation delay, and Doppler, etc. For ISAC systems based on orthogonal frequency division

multiplexing (OFDM) waveforms, the periodogram [11] [12] algorithm is a practical method for parameter estimation. Besides, spectral-based algorithms such as Multiple Signal Classification (MUSIC) [13] and Estimation of Signal Parameters via Rotational Invariance Techniques (ESPRIT) [14] are classical algorithms to achieve super-resolution, for which super-resolution was initially defined as a resolution exceeding the Rayleigh limit for AoA estimation [15]. This concept can be further extended to delay and Doppler estimation, which means a resolution exceeding that achieved by the traditional DFT-based algorithms limited by the bandwidth and duration of the radar signal [16]. Specifically, MUSIC algorithm manipulates the signal autocorrelation matrix to yield noise and signal subspaces, and super-resolution is achieved by exploiting the orthogonality between the two subspaces. However, in spite of the super-resolution ability, MUSIC algorithm suffers from extremely high computational complexity for spectral search and it is most effective only for relatively high signal-to-noise ratio (SNR). On the other hand, super-resolution is achieved by ESPRIT algorithm via exploiting the rotational invariance of the array structure, thus reducing the computational complexity by avoiding spectrum search.

In this paper, we propose the concept of integrated super-resolution sensing and communication (ISSAC), where a common waveform is used for both communication and sensing, and super-resolution algorithm is used for radar signal processing to achieve extreme sensing performance. In particular, we consider the practical fifth generation (5G) New Radio (NR) OFDM waveforms for ISSAC. Note that while OFDM waveforms have been extensively investigated for ISAC systems [12], [17]–[20], these works did not consider implementation in practical communication scenario such as 5G NR. On the other hand, [21] [22] applied super-resolution algorithms to 5G NR ISAC system, but the signals were modeled as standard OFDM waveforms, ignoring the existence of uneven cyclic prefix (CP) in practical 5G NR waveforms. To be more specific, it was specified in 3GPP TS 38.211 [23] that the lengths of CPs in 5G NR OFDM symbols are different in general. For super-resolution sensing algorithms, such an uneven CP length may cause extra phase jumps in the

symbol (slow-time) domain, which may lead to severe bias and increased variance in Doppler estimation, especially when the target velocity is high.

To deal with the above issue, three methods are investigated in this paper to mitigate the influence of uneven CPs in 5G NR waveforms. The first method ignores the extra phase jump caused by long CPs by applying sensing algorithms as if all OFDM symbols had normal CPs. The second method takes into account the existence of long CPs by assuming that all OFDM symbol lengths are equal to the average length of OFDM symbols in a frame. The third method considers the exact structure of OFDM symbols in 5G NR waveforms. Furthermore, we set up an ISSAC prototype system based on 5G NR waveform, which includes Universal Software Radio Peripheral (USRP), millimeter Wave (mmWave) phased array, high precision slide rail and metal plate. The experimental results show that with the properly selected method proposed above, only subtle performance degradation will be caused by unequal CP length when estimating delay and Doppler using 5G NR waveforms.

It is worth mentioning that some relevant experiments on ISAC [24] [25] have been performed to verify the trade off between communication and sensing performance. The authors in [26] introduced MIMO radar based on OFDM waveform for high-resolution synthetic aperture radar (SAR) imaging and data transmission. ISAC systems were also built to verify the performance improvements based on time-division mode [27], [28] and frequency-division mode [29], respectively. Different from such existing works, our current work consider both theoretical analysis and prototyping experiments with super-resolution algorithms based on practical 5G NR waveforms with uneven CPs.

II. SYSTEM MODEL

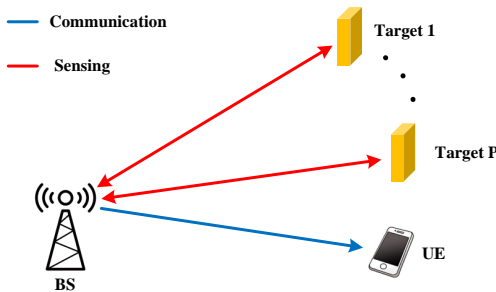


Fig. 1: An ISSAC system based on 5G NR waveform.

We consider an ISSAC system with a dual-functional base station (BS), as shown in Fig. 1. For simplicity, the BS serves one communication user equipment (UE), and simultaneously senses P targets. The standard 5G NR waveform is considered according to 3GPP TS 38.211 [23]. The corresponding waveform parameters for subsequent prototyping experiments in Section IV are specified in Table I, where f_c is the center frequency, B is the bandwidth, μ is the subcarrier spacing

configuration parameter and Δf is the subcarrier spacing. Besides, the number of slots per frame and the number of symbols per slot are denoted by $N_{\text{slot}}^{\text{frame}}$ and $N_{\text{symp}}^{\text{slot}}$, respectively. Therefore, the number of symbols within each frame is $N_{\text{symp}} = N_{\text{slot}}^{\text{frame}} N_{\text{symp}}^{\text{slot}}$. According to 3GPP TS 38.101 [30], the maximum number of Resource Blocks (RB) is denoted as N_{RB} , and each RB contains 12 subcarriers. Therefore, the total number of subcarriers within each RB is $N_{\text{sc}} = 12 \times N_{\text{RB}}$.

TABLE I: 5G NR waveform parameters for ISSAC experiments.

band	FR2 N257
center frequency, f_c	28 GHz
bandwidth, B	400 MHz
subcarrier spacing configuration, μ	3
subcarrier spacing, Δf	120 kHz
slots per frame, $N_{\text{slot}}^{\text{frame}}$	80
symbols per slot, $N_{\text{symp}}^{\text{slot}}$	14
number of symbols per frame, N_{symp}	1120
number of RBs, N_{RB}	264
number of subcarriers, N_{sc}	3168
frame duration	10 ms
slot duration	125 μ s
long CP length	9.4 μ s
normal CP length	8.9 μ s

In 5G NR, the lengths of CP for different OFDM symbols might be different. Therefore, we classify symbols into two types, namely symbols with normal CP and symbols with “long CP”. Note that the term “long CP” is different from the concept of “extended CP” in 5G NR. Extended CP is only used in the configuration of $\mu = 2$, whereas “long CP” exists in 5G NR frames for all configurations.

The structure of the considered 5G NR frame is illustrated in Fig. 2.

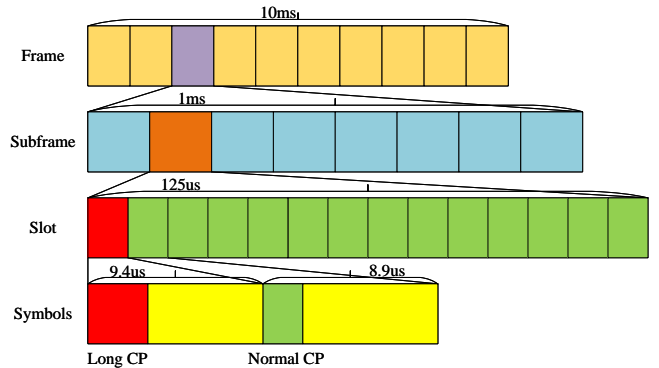


Fig. 2: 5G NR frame structure when $\mu = 3$.

The time-domain waveform of one 5G NR frame can be expressed as

$$s(t) = \sum_{l=0}^{N_{\text{symp}}-1} s_l(t), \quad (1)$$

where $s_l(t)$ is the waveform of the l th OFDM symbol includ-

ing CP, which can be expressed as

$$s_l(t) = \begin{cases} \bar{s}_l(t), & t_{\text{start},l} \leq t < t_{\text{start},l} + T_{\text{symp},l}, \\ 0, & \text{otherwise,} \end{cases} \quad (2)$$

and

$$\bar{s}_l(t) = \sum_{k=0}^{N_{\text{sc}}-1} b_{k,l} e^{j2\pi k \Delta f (t - N_{\text{CP},l} T_c - t_{\text{start},l})}, \quad (3)$$

where $b_{k,l}$ is the information-bearing symbols for communication at the k th subcarrier of the l th symbol. Besides,

$$T_{\text{symp},l} = (N_u + N_{\text{CP},l}) T_c \quad (4)$$

is the length of the l th OFDM symbol including CP, with $N_u = 2048\kappa \cdot 2^{-\mu}$ and $T_c = 1/(\Delta f_{\text{max}} \times N_f)$ denoting the data length of OFDM symbol and the basic time unit for NR, respectively, with $N_f = 4096$ and $\Delta f_{\text{max}} = 480$ kHz. Thus $T_c = 2.0345$ ns. $N_{\text{CP},l}$ is the CP length of the l th OFDM symbol, which can be expressed as

$$N_{\text{CP},l} = \begin{cases} 144\kappa \cdot 2^{-\mu} + 16\kappa & l = 0 \quad \text{or} \quad l = 7 \cdot 2^\mu, \\ 144\kappa \cdot 2^{-\mu} & l \neq 0 \quad \text{and} \quad l \neq 7 \cdot 2^\mu, \end{cases} \quad (5)$$

where $\kappa = T_s/T_c = 64$ is a constant, with $T_s = 1/(\Delta f_{\text{ref}} \times N_{f,\text{ref}})$ denoting the basic time unit for LTE, in which $\Delta f_{\text{ref}} = 15$ kHz and $N_{f,\text{ref}} = 2048$. It is observed from (5) that the CP lengths are uneven in 5G NR. Specifically, for the considered configuration of $\mu = 3$, there is one OFDM symbol with long CP in every 56 OFDM symbols. Therefore, $\eta = 7 \times 2^\mu$ is defined as the separation for adjacent long CPs. Besides, $t_{\text{start},l}$ in (2) denotes the start time of the l th OFDM symbol, given by

$$t_{\text{start},l} = \begin{cases} 0 & l = 0, \\ t_{\text{start},l-1} + T_{\text{symp},l-1} & \text{otherwise.} \end{cases} \quad (6)$$

With the transmitted signal (1), the received echo signal by the BS due to target reflection can be expressed as

$$y(t) = \sum_{p=1}^P \alpha_p s(t - \tau_p) e^{j2\pi f_p t} + w(t), \quad (7)$$

where α_p is the reflection coefficient that includes the impact of radar cross section (RCS) of the p th target, τ_p and f_p denote the propagation delay and the Doppler frequency of the p th target, respectively. Once these two parameters are estimated, the target distance and radial velocity can be obtained as $d_p = c_0 \tau_p / 2$ and $v_p = (f_p c_0) / (2f_c)$, where c_0 denotes the speed of light. $w(t)$ is the independent and identically distributed (i.i.d.) Additive White Gaussian Noise (AWGN) with power spectral density N_0 . At the UE side, the communication process is carried out based on the standard OFDM receiver, and the detail will not be discussed here as we focus on the sensing performance of the ISSAC system.

We assume that the maximum delay does not exceed the CP length, so that after CP removal, $y(t)$ can be rearranged into a $K \times L$ matrix \mathbf{Y} by performing the Fast Fourier Transform (FFT) algorithm [12], with K and L denoting the number of subcarriers and symbols, respectively. Therefore, the (k, l) th element of \mathbf{Y} can be expressed as

$$\mathbf{Y}(k, l) = b_{k,l} \sum_{p=1}^P \alpha_p e^{-j2\pi k \tau_p \Delta f} e^{j2\pi f_p T_{\text{sum},l}} + w_{k,l}, \quad (8)$$

in which $T_{\text{sum},l}$ is the cumulative durations at the l th symbol, Based on (4) and (5), $T_{\text{sum},l}$ can be expressed as

$$\begin{aligned} T_{\text{sum},l} &= \sum_{i=0}^l T_{\text{symp},i} \\ &= (N_u + 144\kappa \times 2^{-\mu}) T_c l + 16\kappa T_c \left\lceil \frac{l}{\eta} \right\rceil, \end{aligned} \quad (9)$$

where $\lceil x \rceil$ denotes the minimum integer no less than x . Furthermore, by dividing the random communication symbols $b_{k,l}$ and substituting (9) into (8), the data matrix $\tilde{\mathbf{Y}}$ for radar processing can be obtained as:

$$\begin{aligned} \tilde{\mathbf{Y}}(k, l) &= \frac{\mathbf{Y}(k, l)}{b_{k,l}} = \sum_{p=1}^P \alpha_p e^{-j2\pi k \tau_p \Delta f} e^{j2\pi f_p T_{\text{sum},l}} + \tilde{w}_{k,l} \\ &= \sum_{p=1}^P \alpha_p e^{-j2\pi k \tau_p \Delta f} e^{j2\pi f_p (N_u + 144\kappa \times 2^{-\mu}) T_c l} e^{j2\pi f_p 16\kappa T_c \lceil \frac{l}{\eta} \rceil} \\ &\quad + \tilde{w}_{k,l}. \end{aligned} \quad (10)$$

Different from the standard OFDM model [12] [31], due to the existence of long CP of 5G NR waveforms, there is an additional phase shift $\Delta\phi = 2\pi f_p 16\kappa T_c \lceil \frac{l}{\eta} \rceil$ in (10), which is generally small and no longer increase linearly with the symbol index l . For the waveform specified in Table I, by substituting $l \leq N_{\text{symp}} - 1$ and $\Delta f = 120$ kHz, we have $|\Delta\phi| \leq \pi/4$ if $|f_p| \leq \frac{1}{10} \Delta f$. Such an additional phase shift may cause bias in Doppler estimation, which has not been considered in traditional OFDM radar processing. In this paper, three methods are investigated to deal with the above issue:

- 1) In the first method, the existence of long CPs in the NR OFDM frame and the extra phase jumps caused by it are not considered at all, which means the lengths of all OFDM symbols are considered equal to the length of OFDM symbols with normal CPs. In this way, $T_{\text{sum},l}$ can be expressed as:

$$T_{\text{sum},l}^{\text{I}} = (N_u + 144\kappa \times 2^{-\mu}) T_c l. \quad (11)$$

- 2) In the second method, the extra phase introduced by long CPs is approximated by assuming that all symbols have the same length, which is equal to the average symbol length of each OFDM symbol in a frame. $T_{\text{sum},l}$ is chosen to be the average of all symbol lengths of an NR OFDM frame with duration $T_{\text{frame}} = 10$ ms:

$$T_{\text{sum},l}^{\text{II}} = T_{\text{frame}} l / N_{\text{symp}}. \quad (12)$$

- 3) In the third method, the exact structure of the NR OFDM frame with long CPs is considered, as shown in (9). Considering the different principles for different sensing algorithms, the specific countermeasures taken will vary depending on the chosen algorithm, which will be discussed in detail in the next section.

In the following, three classical sensing algorithms are modified based on the three methods above to mitigate the influence of uneven CPs.

III. SUPER-RESOLUTION SENSING ALGORITHM WITH UNEVEN CP

In this section, three classic sensing algorithms, namely Periodogram, MUSIC and ESPRIT are studied to estimate the delay and Doppler parameters based on 5G NR waveforms. The Periodogram algorithm serves as the baseline for the super-resolution algorithms in ISSAC system. Firstly, we introduce the principles and implementation methods of the different algorithms. Furthermore, we perform three algorithms on $\tilde{\mathbf{Y}}$ to estimate the delay and Doppler parameter, and analyze the impact of uneven CP in 5G NR waveforms on different algorithms, respectively.

A. Periodogram

In this subsection, the one-dimensional Periodogram [12] is performed in the delay and Doppler domain as a baseline of super-resolution sensing algorithms. The FFT and IFFT are applied to each row and column of $\tilde{\mathbf{Y}}$, and their Periodogram can be expressed as:

$$\begin{aligned} \bar{y}_f &= \sum_{k=1}^{N_{sc}} \frac{1}{N_{sc}N_{\text{symp}}} \left| \text{FFT}_{N_{\text{symp}}^{\text{FFT}}}(\tilde{\mathbf{y}}_k) \right|^2, \\ \bar{y}_\tau &= \sum_{l=1}^{N_{\text{symp}}} \frac{1}{N_{sc}N_{\text{symp}}} \left| \text{IFFT}_{N_{sc}^{\text{FFT}}}(\tilde{\mathbf{y}}_l^T) \right|^2, \end{aligned} \quad (13)$$

where $\tilde{\mathbf{y}}_n$ and $\tilde{\mathbf{y}}_n^T$ denotes the n th row and column of matrix $\tilde{\mathbf{Y}}$, respectively. The peaks of \bar{y}_f and \bar{y}_τ correspond to the Doppler and delay of the targets, respectively. N_{sc}^{FFT} and $N_{\text{symp}}^{\text{FFT}}$ are the number of points for fast Fourier transforms. It is assumed that each symbol in OFDM frame has the same length T_{symp} , and the Doppler and delay of the target can be solved by the peak index n_f and n_τ of the periodogram:

$$f = \frac{n_f}{N_{\text{symp}}^{\text{FFT}} T_{\text{symp}}}, \quad \tau = \frac{n_\tau}{N_{sc}^{\text{FFT}} \Delta f}. \quad (14)$$

The delay and Doppler resolutions of the Periodogram algorithm are limited by the signal duration and bandwidth. Therefore, a trade-off between resolution and maximum measurement range needs to be considered [32]. Note that in Periodogram, the long CP introduces a slight phase shift in the symbol (slow-time) domain. Therefore, we design three signal processing methods for Periodogram according to Section II. In particular, for method 3, the symbol structure is no longer uniform, so the traditional FFT is no longer applicable. We construct matched filter by substituting (14):

$$\mathbf{F}(n, m) = e^{\frac{-j2\pi n T_{\text{sum},m}}{N_{\text{symp}}^{\text{FFT}} T_{\text{sum},1}}}, \quad (15)$$

where $n, m = 1, \dots, N_{\text{symp}}^{\text{FFT}}$. The periodogram of the matched filter is

$$\bar{y}_f = \sum_{k=1}^{N_{sc}} \frac{1}{N_{sc}N_{\text{symp}}} |\mathbf{F}\tilde{\mathbf{y}}_k|^2. \quad (16)$$

Fig. 3 shows the simulation results of the three methods of the Periodogram, and the black dotted line represents the ground truth. There are two targets with the speed of $v_1 = 63.75$ m/s and $v_2 = 64.29$ m/s, corresponding to Doppler frequencies $f_1 = 11.90$ kHz and $f_2 = 12.00$ kHz, respectively. It can be seen that method 1 leads to obvious bias

in estimation, while methods 2 and 3 are unbiased. However, due to the poor resolution of the Periodogram, methods 2 and 3 fail to show notable difference between each other.

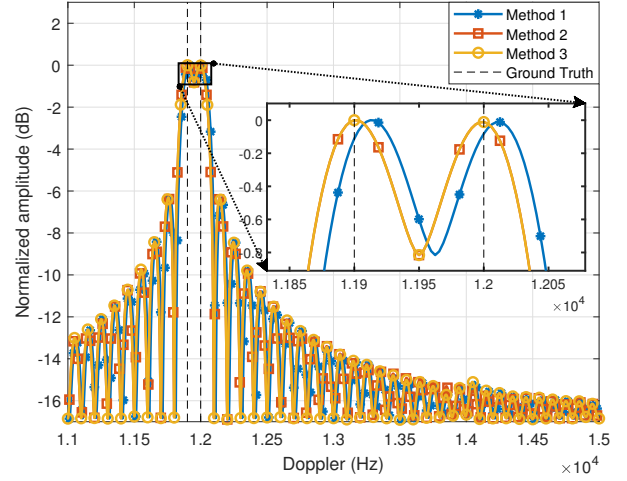


Fig. 3: Periodogram simulation result.

B. MUSIC

In this subsection, we study the classic MUSIC algorithm on the $N_{sc} \times N_{\text{symp}}$ data matrix $\tilde{\mathbf{Y}}$ and analyze the effect of uneven CPs on the estimation results. Due to the limited length of measurement data and high correlation between reflected signals, the covariance matrix of $\tilde{\mathbf{Y}}$ may be rank deficient. Therefore, we perform modified spatial smoothing preprocessing (MSSP) [33] in the subcarrier domain. Note that no preprocessing in the symbol domain is performed to avoid the destruction of the uneven structure between symbols. To be more specific, N_{sub} submatrices of size $L \times N_{\text{symp}}$ are selected in all the N_{sc} subcarriers, where $N_{\text{sub}} = N_{sc} - L + 1$, $L = \rho N_{sc}$ and $\rho = 0.4$ is the smoothing constant, and the $L \times N_{\text{sub}} N_{\text{symp}}$ data matrix after MSSP can be expressed as:

$$\hat{\mathbf{Y}} = \begin{pmatrix} \tilde{\mathbf{y}}_1 & \cdots & \tilde{\mathbf{y}}_{N_{\text{sub}}} \\ \vdots & \ddots & \vdots \\ \tilde{\mathbf{y}}_L & \cdots & \tilde{\mathbf{y}}_{L+N_{\text{sub}}} \end{pmatrix}. \quad (17)$$

Furthermore, the eigenvalue decomposition is performed on the covariance matrix of Doppler and delay \mathbf{R}_f and \mathbf{R}_τ , respectively:

$$\mathbf{R}_f = \frac{\hat{\mathbf{Y}}^H \hat{\mathbf{Y}}}{N_{sc}} = \mathbf{E}_s^f \mathbf{\Lambda}_s^f (\mathbf{E}_s^f)^H + \mathbf{E}_n^f \mathbf{\Lambda}_n^f (\mathbf{E}_n^f)^H, \quad (18)$$

$$\mathbf{R}_\tau = \frac{\hat{\mathbf{Y}} \hat{\mathbf{Y}}^H}{N_{\text{sub}} N_{\text{symp}}} = \mathbf{E}_s^\tau \mathbf{\Lambda}_s^\tau (\mathbf{E}_s^\tau)^H + \mathbf{E}_n^\tau \mathbf{\Lambda}_n^\tau (\mathbf{E}_n^\tau)^H,$$

where $\mathbf{\Lambda}_s^q$ denotes the diagonal matrix with respect to the P largest eigenvalues, and \mathbf{E}_s^q and \mathbf{E}_n^q denote the signal subspace and noise subspace respectively, with $q \in \{\tau, f\}$.

Therefore, the MUSIC spectrum can be obtained as:

$$P_f^{\text{MUSIC}}(f) = \frac{1}{(\mathbf{x}^f)^H \mathbf{E}_n^f (\mathbf{E}_n^f)^H \mathbf{x}^f}, \quad (19)$$

$$P_\tau^{\text{MUSIC}}(\tau) = \frac{1}{(\mathbf{x}^\tau)^H \mathbf{E}_n^\tau (\mathbf{E}_n^\tau)^H \mathbf{x}^\tau},$$

$$\mathbf{x}^f = [x_0^f, \dots, x_{N_{\text{syemb}}-1}^f]^T, \quad (20)$$

$$\mathbf{x}^\tau = [x_0^\tau, \dots, x_{L-1}^\tau]^T,$$

where $x_l^f = e^{j2\pi f T_{\text{syemb},l}}$ and $x_k^\tau = e^{-j2\pi k \tau \Delta f}$ denote the l th and k th element of the Doppler and delay steering vectors, respectively. In the following, the effect of uneven CP on MUSIC algorithm is analyzed in the Doppler domain. Three Doppler steering vector are designed corresponding to the three methods in Section II, where we have $T_{\text{syemb},l} = T_{\text{sum},l}$ for the third method.

Fig. 4 shows the simulation result of MUSIC algorithm based on three different methods above, where the black dotted line is the true Doppler frequency. There are two targets with the speed of $v_1 = 64.18$ m/s and $v_2 = 64.29$ m/s, corresponding to Doppler frequencies $f_1 = 11.98$ kHz and $f_2 = 12.00$ kHz, respectively. As can be seen from the figure, if the structure of long CP is not considered, severe deviations occur at the MUSIC spectrum peaks when the Doppler frequencies of the two targets are close. Method 2 can reduce the deviation of Doppler estimation, but the resolution of the two spectrum peaks is still poor. Furthermore, with method 3, the orthogonality between the steering vectors and the noise subspace is enhanced, so the estimation result is accurate with the highest resolution.

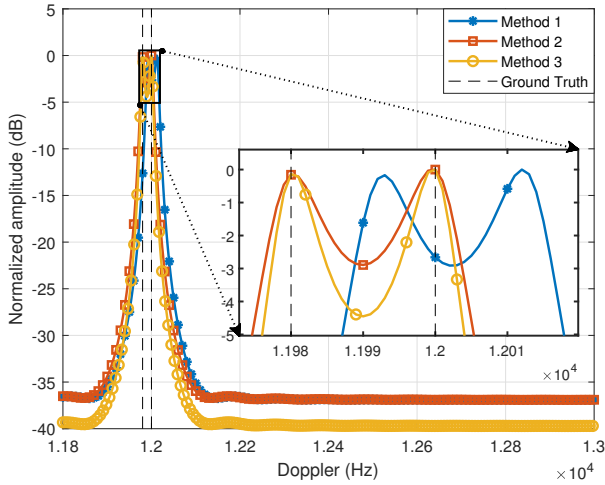


Fig. 4: MUSIC simulation result.

C. ESPRIT

In conventional OFDM radar, the ESPRIT algorithm is used to estimate delay based on the rotational invariance between OFDM signal subcarriers. It can also be used to estimate the

Doppler by exploiting the uniform structure between multiple OFDM symbols [17].

The ESPRIT algorithm first needs to select two sub-sequences with a fixed phase shift from the signal subspace, that is, sub-sequences with rotational invariance. This phase shift is called the rotational invariant factor, and this factor can be used to estimate the frequency shift. Since no spectrum peak search is required, its complexity is much lower than that of MUSIC algorithm. However, ESPRIT algorithm requires strictly uniform structure between elements of sub-sequences.

Similar to MUSIC algorithm, the Doppler and delay domain covariance matrix are obtained according to (18). The eigenvalue decomposition is performed to obtain the signal subspace \mathbf{E}_s^f and \mathbf{E}_s^τ . After that, we select two $(N_{\text{syemb}} - 1) \times P$ submatrices from the Doppler signal subspace \mathbf{E}_s^f and two $(N_{\text{sc}} - 1) \times P$ submatrices from the delay signal subspace \mathbf{E}_s^τ to maintain rotational invariance.

$$\mathbf{J}_{f,1} = [\mathbf{E}_{s,1}^f, \dots, \mathbf{E}_{s,N_{\text{syemb}}-1}^f]^T, \mathbf{J}_{f,2} = [\mathbf{E}_{s,2}^f, \dots, \mathbf{E}_{s,N_{\text{syemb}}}^f]^T$$

$$\mathbf{J}_{\tau,1} = [\mathbf{E}_{s,1}^\tau, \dots, \mathbf{E}_{s,N_{\text{sc}}-1}^\tau]^T, \mathbf{J}_{\tau,2} = [\mathbf{E}_{s,2}^\tau, \dots, \mathbf{E}_{s,N_{\text{sc}}}^\tau]^T, \quad (21)$$

where $\mathbf{E}_{s,i}^q$ denotes the i th row of the signal subspace. Based on the rotational invariance of uniform structure, the rotation invariant matrices of two dimensions are obtained from the submatrices as $\Phi = (\mathbf{J}_{f,2}^H \mathbf{J}_{f,1})^{-1} \mathbf{J}_{f,2}^H \mathbf{J}_{f,1}$ and $\Psi = (\mathbf{J}_{\tau,2}^H \mathbf{J}_{\tau,1})^{-1} \mathbf{J}_{\tau,2}^H \mathbf{J}_{\tau,1}$. Then, the delay and Doppler of multiple targets can be solved by the eigenvalue of $\Phi = \mathbf{U}_f^{-1} \mathbf{D}_f \mathbf{U}_f$ and $\Psi = \mathbf{U}_\tau^{-1} \mathbf{D}_\tau \mathbf{U}_\tau$, where

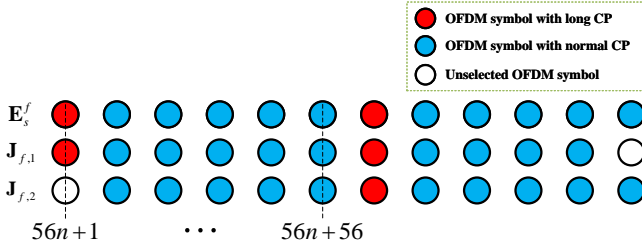
$$\mathbf{D}_f = \text{diag}(e^{-j2\pi f_1 T_{\text{syemb}}}, \dots, e^{-j2\pi f_P T_{\text{syemb}}}),$$

$$\mathbf{D}_\tau = \text{diag}(e^{-j2\pi \tau_1 \Delta f}, \dots, e^{-j2\pi \tau_P \Delta f}). \quad (22)$$

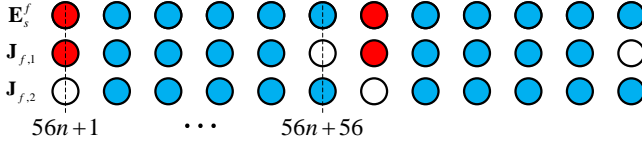
However, the uneven CP of NR waveform may destroy the uniform structure between symbols, and thus degrade the accuracy of the Doppler estimation using ESPRIT algorithm. Similar to the analysis in Section II, three different method are considered for \mathbf{D}_f . In method 3, we propose a non-uniform ESPRIT solution, which is able to eliminate the effect of uneven CP while maintaining the rotation invariance of the two selected subarrays by removing the elements associated with the long CP symbols from the signal subspace. To be more specific, $\mathbf{J}_{f,1}$ is selected by removing the $(\eta n + \eta)$ th row from \mathbf{E}_s^f , and $\mathbf{J}_{f,2}$ is obtained by removing the $(\eta n + 1)$ th row from \mathbf{E}_s^f , where $n = (0, \dots, N_{\text{syemb}}/\eta - 1)$.

Fig. 5 compares the conventional and proposed signal subspace submatrix of ESPRIT algorithm, denoted by the upper part and the lower part, respectively. Each row represents the transposed matrix of \mathbf{E}_s^f , and each circle represents a row of \mathbf{E}_s^f . The red circle is the row where the long CP is located in the signal subspace, the blue circle is the row of other OFDM symbols and the white circle is the removed row of \mathbf{E}_s^f .

Fig. 6 shows the estimation result of ESPRIT algorithm running 100 times in each method at SNR of 15 dB, where the black dashed line is the true Doppler frequency. There are two targets with the speed of $v_1 = 63.75$ m/s and $v_2 = 64.29$ m/s, corresponding to Doppler frequencies $f_1 = 11.90$ kHz and $f_2 = 12.00$ kHz, respectively. It can be seen that there is a



(a) Conventional ESPRIT



(b) Proposed non-uniform ESPRIT

Fig. 5: The selected signal subspace submatrix of conventional ESPRIT versus the proposed non-uniform ESPRIT.

significant deviation between the estimation result and the true value for method 1, when long CP is not considered. Besides, using average symbol length can improve the estimation accuracy. Furthermore, considering the effect of long CP in method 3, the accuracy can be increased as well, but the variance is larger than method 2 due to the reduction of array size and low SNR. This shows that in ESPRIT algorithm, the loss of array size has a greater impact on the algorithm than the loss of rotation invariance. Therefore, method 2 is used for subsequent experimental data processing. We do not consider the spatial smoothing before Doppler estimation because of the existence of long CP, which is similar to method 3 considering non-uniform smoothing matrices.

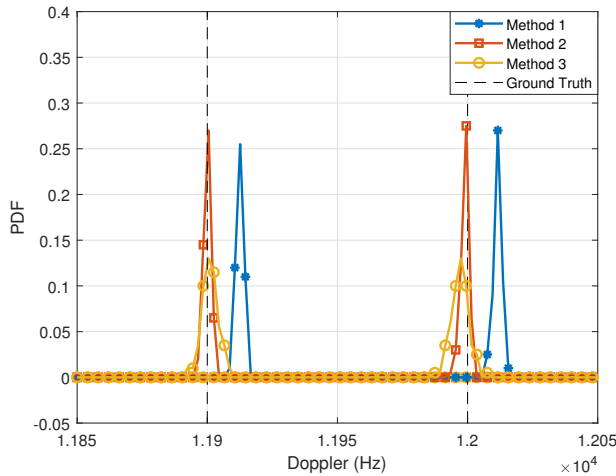


Fig. 6: ESPRIT simulation result.

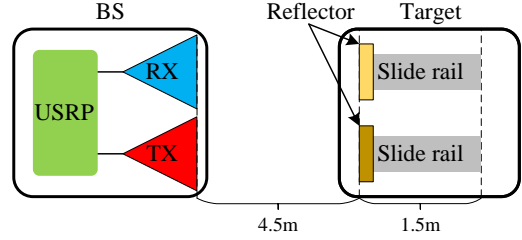


Fig. 7: Experimental setup.

IV. PROTOTYPING EXPERIMENTS AND RESULTS

A. Experimental Setup

In this section, we validate our developed results with prototyping experiments. The ISSAC experimental platform consists of a BS and a pair of high-precision slide rail with fixed metal plates as the sensing targets, as shown in Fig. 7.

A PXIe 8881 is used as a controller at the BS side, which is responsible for 5G NR waveform configuration and generation, radar signal processing, etc. Universal Software Radio Peripheral (USRP) X410 is used for the transmission and reception of the Intermediate Frequency (IF) signals. The working frequency of X410 ranges from 1 MHz to 7.2 GHz, and the maximum supported bandwidth is 400 MHz. An IF frequency of 2.8 GHz and a bandwidth of 400 MHz are chosen. Four RF channels are available on the X410 and two of them are connected to a pair of 8×8 millimeter wave (mmWave) phased arrays with embedded mmWave up and down converters. The up and down converters convert the 2.8 GHz IF signals to and from 28 GHz mmWave signals. For this work, we focus on range and Doppler sensing, and the mmWave beams are configured to point towards the targets. The equivalent isotropically radiated power (EIRP) is configured to be 44 dBm. As shown in Fig. 7 and Fig. 8, two 1.5 m-long slide rails are placed 4.5 m away from the BS. Two metal plates are placed on the slide rails with varying positions to mimic the sensing targets. In the following, the delay and Doppler of the targets are estimated.

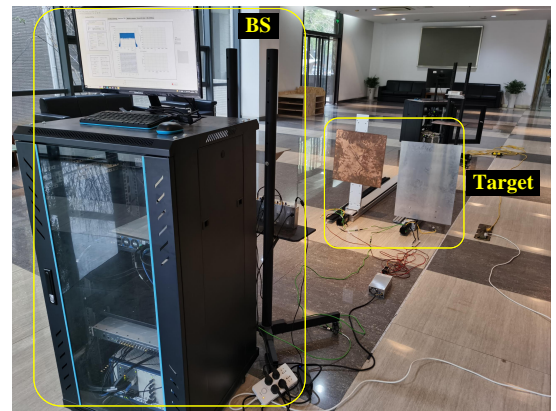


Fig. 8: Prototyping experiment scenarios for ISSAC.

B. Delay Estimation

We first control the sliding rails to place the targets at a set of fixed distances shown in Table II. The BS sends a downlink NR frame to initiate the measurement. After finishing the measurement, the BS implements the three sensing algorithms discussed in Section III to process the received data.

The performance of delay estimation for the three algorithms is shown in Fig. 9 by evaluating the resolution in terms of various distance differences between the two targets. Fig. 9a and Fig. 9b plot the search spectra versus distance with varying range differences for Periodogram and MUSIC respectively, while Fig. 9c plots the results of five estimations for ESPRIT. It can be seen that the MUSIC and ESPRIT algorithms can achieve a more accurate estimation than the Periodogram. Furthermore, when the distance difference between targets is small, e.g., 0.4 m, Periodogram fails to distinguish the two targets, while MUSIC and ESPRIT algorithms can resolve the nearby targets, showing their super-resolution capability.

TABLE II: Distance of targets

Experiment	Distance 1	Distance 2	Distance difference, Δd
1	4.5 m	5.7 m	1.2 m
2	4.7 m	5.5 m	0.8 m
3	4.9 m	5.3 m	0.4 m

C. Doppler Estimation

To illustrate velocity estimation, the sliding rails are controlled to move the targets at different speeds, as shown in Table III. Limited by hardware conditions, the maximum speed of the sliding rail is 0.18 m/s. Similar to the delay estimation experiment, the BS sends a downlink NR frame to initiate the measurements. After completing the measurements, the BS uses Periodogram, the method 3 of MUSIC and the method 2 of ESPRIT to process the data, respectively.

Fig. 10 shows the performance of the three algorithms in terms of the difference between the velocity of the two targets.

It is observed that for the Periodogram algorithm, the velocity resolution is so poor that none of the targets can be distinguished at such low speed. By contrast, the MUSIC and ESPRIT algorithms can resolve the two targets with small velocity difference, except when the difference is too small, e.g., 0.10 m/s.

TABLE III: Velocity of targets

Experiment	Velocity 1	Velocity 2	Velocity difference, Δv
1	0	0.18 m/s	0.18 m/s
2	0.02 m/s	0.16 m/s	0.14 m/s
3	0.04 m/s	0.14 m/s	0.10 m/s

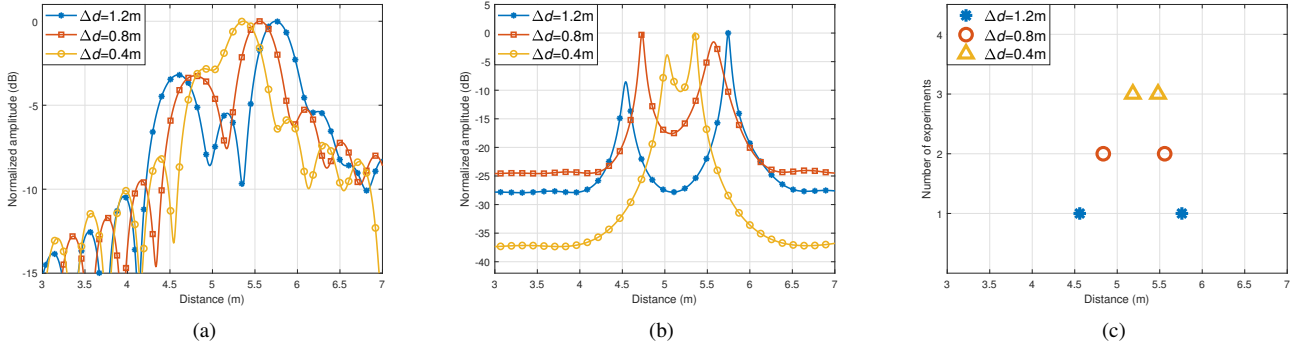


Fig. 9: Experiment results with varying distance difference by using Periodogram (a), MUSIC (b) and ESPRIT (c).

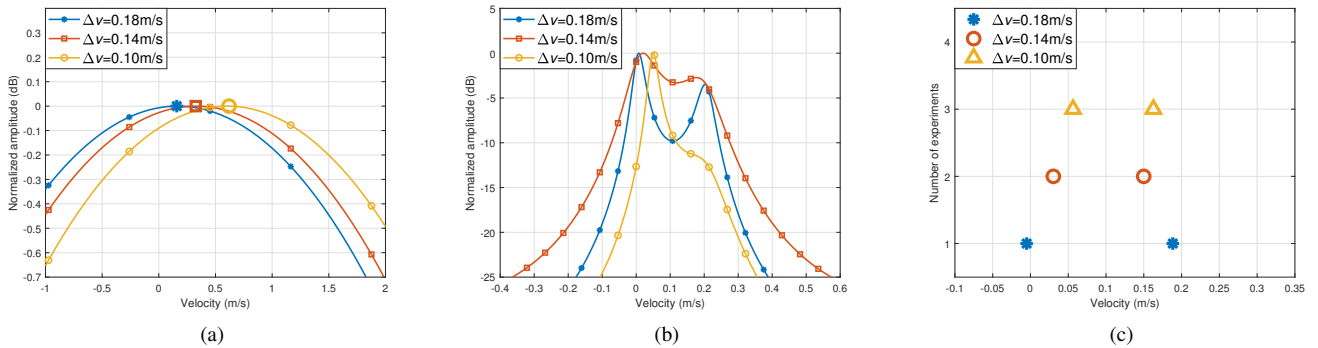


Fig. 10: Experiment results with varying velocity difference by using Periodogram (a), MUSIC (b) and ESPRIT (c).

V. CONCLUSION

In this paper, we propose the concept of ISSAC based on 5G NR waveform, and study the signal processing methods with uneven CPs, including Periodogram, MUSIC and ESPRIT. The impact of uneven CPs on various sensing algorithms for Doppler estimation is studied, and three methods are investigated to resolve the issue. Finally, an ISSAC experimental platform is built, and two targets with different distance and speed differences are sensed by the ISSAC BS. The results show that the two super-resolution algorithms, namely MUSIC and ESPRIT, can significantly improve the delay and Doppler resolution as compared to Periodogram algorithm.

ACKNOWLEDGEMENT

This work was supported by the National Key R&D Program of China with Grant number 2019YFB1803400 and by the Natural Science Foundation of China under Grant 62071114.

REFERENCES

- [1] F. Liu, Y. Cui, C. Masouros, J. Xu, T. X. Han, Y. C. Eldar, and S. Buzzi, "Integrated sensing and communications: Towards dual-functional wireless networks for 6g and beyond," *IEEE J. Sel. Areas Commun.*, 2022.
- [2] F. Liu, C. Masouros, T. Ratnarajah, and A. Petropulu, "On range sidelobe reduction for dual-functional radar-communication waveforms," *IEEE Wireless Commun. Lett.*, vol. 9, no. 9, pp. 1572–1576, 2020.
- [3] Z. Xiao and Y. Zeng, "Waveform design and performance analysis for full-duplex integrated sensing and communication," *IEEE J. Sel. Areas Commun.*, vol. 40, no. 6, pp. 1823–1837, 2022.
- [4] R. Li, Z. Xiao, and Y. Zeng, "Beamforming towards seamless sensing coverage for cellular integrated sensing and communication," in *Proc. IEEE Int. Conf. Commun. Workshops (ICC Workshops)*. IEEE, 2022, pp. 492–497.
- [5] H. Hua, J. Xu, and T. X. Han, "Optimal transmit beamforming for integrated sensing and communication," *IEEE Transactions on Vehicular Technology*, 2023.
- [6] S. Chen, Z. Xiao, and Y. Zeng, "Simultaneous beam sweeping for multi-beam integrated sensing and communication," in *Proc. IEEE Int. Conf. Commun. (ICC)*, 2022, pp. 4438–4443.
- [7] I. S. Gradshteyn and I. M. Ryzhik, *Table of integrals, series, and products*. Academic press, 2014.
- [8] M. Kobayashi, G. Caire, and G. Kramer, "Joint state sensing and communication: Optimal tradeoff for a memoryless case," in *Proc. IEEE Int. Symp. Inf. Theor. Proc.*, 2018, pp. 111–115.
- [9] H. Wang, Z. Xiao, and Y. Zeng, "Cramér-rao bounds for near-field sensing with extremely large-scale MIMO," *arXiv preprint arXiv:2303.05736*, 2023.
- [10] H. Wang and Y. Zeng, "SNR scaling laws for radio sensing with extremely large-scale MIMO," in *Proc. IEEE Int. Conf. Commun. Workshops (ICC Workshops)*, 2022, pp. 121–126.
- [11] C. Sturm, "Joint implementation of communication and radar based on OFDM," Ph.D. dissertation, Karlsruhe Institute of Technology, 2011.
- [12] K. M. Braun, "OFDM radar algorithms in mobile communication networks," Ph.D. dissertation, Karlsruhe, Karlsruher Institut für Technologie (KIT), Diss., 2014.
- [13] W. Li and W. Liao, "Conditioning of restricted fourier matrices and super-resolution of MUSIC," in *Int. Conf. Sampl. Theory Appl., SampTA*. IEEE, 2019, pp. 1–4.
- [14] R. Roy and T. Kailath, "ESPRIT-estimation of signal parameters via rotational invariance techniques," *IEEE Trans. Acoust., Speech, Signal Process.*, vol. 37, no. 7, pp. 984–995, 1989.
- [15] E. Gonen and J. M. Mendel, "Subspace-based direction finding methods," *The digital signal processing handbook*, vol. 62, 1999.
- [16] P. Peebles, Jr., *Radar Principles*. John Wiley and Sons Inc., 1998.
- [17] D. H. Nguyen and R. W. Heath, "Delay and doppler processing for multi-target detection with IEEE 802.11 OFDM signaling," in *2017 ICASSP IEEE Int. Conf. Acoust. Speech Signal Process Proc.* IEEE, pp. 3414–3418.
- [18] L. Zheng and X. Wang, "Super-resolution delay-doppler estimation for OFDM passive radar," *IEEE Trans. Signal Process.*, vol. 65, no. 9, pp. 2197–2210, 2017.
- [19] R. Xie, D. Hu, K. Luo, and T. Jiang, "Performance analysis of joint range-velocity estimator with 2d-music in OFDM radar," *IEEE Trans. Signal Process.*, vol. 69, pp. 4787–4800, 2021.
- [20] Z. Wei, H. Qu, Y. Wang, X. Yuan, H. Wu, Y. Du, K. Han, N. Zhang, and Z. Feng, "Integrated sensing and communication signals towards 5G-A and 6G: A survey," *IEEE Internet Things J.*, pp. 1–1, 2023.
- [21] M. Henninger, S. Mandelli, M. Arnold, and S. Ten Brink, "A computationally efficient 2D music approach for 5G and 6G sensing networks," in *2022 IEEE Wireless Commun. Networking Conf. WCNC*. IEEE, 2022, pp. 210–215.
- [22] L. Pucci, E. Matricardi, E. Paolini, W. Xu, and A. Giorgetti, "Performance analysis of joint sensing and communication based on 5G new radio," in *2021 IEEE Globecom Workshops (GC Wkshps)*. IEEE, 2021, pp. 1–6.
- [23] 3GPP, "NR; Physical channels and modulation," 3rd Generation Partnership Project (3GPP), Technical Specification (TS) 38.211, 01 2023, version 17.4.0.
- [24] T. Xu, F. Liu, C. Masouros, and I. Darwazeh, "An experimental proof of concept for integrated sensing and communications waveform design," *IEEE open J. Commun. Soc.*, vol. 3, pp. 1643–1655, 2022.
- [25] M. Temiz, C. Horne, N. J. Peters, M. A. Ritchie, and C. Masouros, "An experimental study of radar-centric transmission for integrated sensing and communications," *IEEE Trans. Microw. Theory Techn.*, pp. 1–14, 2023.
- [26] J. Wang, X.-D. Liang, L.-Y. Chen, L.-N. Wang, and K. Li, "First demonstration of joint wireless communication and high-resolution sar imaging using airborne MIMO radar system," *IEEE Trans. Geosci. Remote Sens.*, vol. 57, no. 9, pp. 6619–6632, 2019.
- [27] Q. Zhang and X. Gao, "Joint communication and sensing enabled cooperative perception testbed for connected automated vehicles," in *INFOCOM WKSHPs 2022 - IEEE Conf. Comput. Commun. Workshops*, 2022, pp. 1–2.
- [28] D. Ma, N. Shlezinger, T. Huang, Y. Shavit, M. Namer, Y. Liu, and Y. C. Eldar, "Spatial modulation for joint radar-communications systems: Design, analysis, and hardware prototype," *IEEE Trans. Veh. Technol.*, vol. 70, no. 3, pp. 2283–2298, 2021.
- [29] J. Moghaddasi and K. Wu, "Multifunctional transceiver for future radar sensing and radio communicating data-fusion platform," *IEEE Access*, vol. 4, pp. 818–838, 2016.
- [30] 3GPP, "NR; Physical layer; General description," 3rd Generation Partnership Project (3GPP), Technical Specification (TS) 38.201, 05 2022, version 17.0.0.
- [31] C. Sturm and W. Wiesbeck, "Waveform design and signal processing aspects for fusion of wireless communications and radar sensing," *Proc. IEEE*, vol. 99, no. 7, pp. 1236–1259, 2011.
- [32] C. D. Ozkaptan, E. Ekici, O. Altintas, and C.-H. Wang, "OFDM pilot-based radar for joint vehicular communication and radar systems," in *2018 IEEE Veh. Netw. Conf., VNC*, 2018, pp. 1–8.
- [33] H. Yamada, M. Ohmiya, Y. Ogawa, and K. Itoh, "Superresolution techniques for time-domain measurements with a network analyzer," *IEEE Trans. Antennas Propag.*, vol. 39, no. 2, pp. 177–183, 1991.